Molecular dynamics simulation study of spherical nanoparticles in a nematogenic matrix: Anchoring, interactions, and phase behavior

Jianqing Xu, Dmitry Bedrov, and Grant D. Smith*
Department of Materials Science and Engineering, University of Utah, Salt Lake City, Utah 84112, USA

Matthew A. Glaser
Department of Physics and Liquid Crystal Materials Research Center, University of Colorado, Boulder, Colorado 80309, USA
(Received 25 March 2008; published 14 January 2009)

Molecular dynamics simulations of spherical nanoparticles (NPs) in a nematogenic matrix of soft spherocylinders (SSCs) with equal NP diameter and SSC length were performed. The NPs were found to be dispersed in the isotropic SSC matrix. At higher pressure, the NP-SSC mixture demixed into a NP-poor nematic phase and a NP-rich isotropic phase over most of the composition range investigated. However, at low NP concentrations a single-phase nematic with dispersed NPs was observed, while at very high NP concentration no nematic phase was observed. When the NP-SSC interactions were changed to promote homeotropic anchoring, the matrix-induced interaction between NPs in the isotropic SSC matrix exhibited strong intermediate-range repulsion that was expected to result in even greater dispersion of NPs. However, many-body effects appear to dominate NP-NP interactions in the isotropic SSC matrix with homeotropic anchoring even at the lowest NP concentration investigated, resulting in suppression of the intermediate range repulsion leading to aggregation of the NPs.

DOI: 10.1103/PhysRevE.79.011704 PACS number(s): 61.30.Cz

I. INTRODUCTION

Liquid crystals (LCs) are natural candidates for matrix-guided self-assembly of nanoparticles (NPs) for a wide variety of potential applications [1]. Recent experiments [2–4] as well as theory [5–7] reveal that when mixtures of NPs and nematogenic molecules of comparable size are formed, the aggregation state of the NPs can be strongly modulated by the phase of the LC matrix. Dispersion of the NPs in the LC matrix is observed above the isotropic-nematic transition temperature (T_{IN}) with aggregation associated with phase separation into LC-rich nematic and NP-rich isotropic phases occurring at lower temperatures. Furthermore, unlike colloid-LC mixtures where the particle is much larger than the LC molecules and particle dispersions in nematic LC matrices are metastable [8,9], theory for rod-sphere mixtures [7] as well as experimental studies of nematic LC-isotropic fluid [9] and LC-nanodroplet [2–4] mixtures reveal that when the particle is comparable in size to the nematogen or smaller, the particles have finite solubility in the nematic LC matrix and a stable single-phase nematic with a homogeneous distribution of particles can be realized.

NP-LC mixtures are unique within the generic class of mixtures of spherical and rodlike particles of similar size in the importance of potentially tunable interactions on the nanometer length scale, particularly LC-NP anchoring, i.e., how the LC molecules prefer to orient at the NP surface. In principle, it is possible to influence this anchoring through change in chemical interactions in the NP-LC system, e.g., through NP surface modification, providing an additional "handle" for controlling self-assembly in these intriguing systems. In this paper, we present results from a molecular dynamics (MD) simulation study of the effective interactions and phase behavior of spherical NPs in a mesogenic matrix of soft spherocylinders (SSCs). This model could equally well be regarded as a model for mixtures of spherical and rodlike colloids, and the results are applicable to any system of spherical and rodlike particles of comparable size whose behavior is driven by entropic interactions. In addition, we have investigated the influence of anchoring conditions on matrix-induced NP-NP interactions and phase behavior, thereby bringing the model squarely into the purview of nanoscale interactions.

We note that this work builds on our previous MD simulation studies of spherical NPs in SSCs [10,11]. In that work, we found that the NPs experience a net repulsion in the isotropic phase of the nematogen and remain dispersed in the LC matrix up to the highest volume fraction of NPs investigated. We associated this behavior with a matrix-induced long-range repulsion. Subsequent to those studies, we have discovered two errors in our analysis of the simulation results that have been corrected [12], leading to the conclusion that dispersion of NPs in the isotropic LC matrix is due to short-range interaction only (see also below).

II. SIMULATION METHODOLOGY

The simulation model is described in our previous papers [10,11]. Briefly, nematogens were represented as soft spherocylinders (SSCs) with diameter $D_{\mathrm{SSC}}=\sigma$ and length $L_{\mathrm{SSC}}=5\sigma$ ($L_{\mathrm{SSC}}/D_{\mathrm{SSC}}=5$), as shown in Fig. 1, while the NPs have a hard-core diameter $D_{\mathrm{NP}}=5\sigma$. Interactions are given as

$$U(r)=4\varepsilon\left[\left(\frac{\sigma}{r-R_h}\right)^{12}-\left(\frac{\sigma}{r-R_h}\right)^{6}+\frac{1}{4}\right] \quad \text{for } r-R_h<\sqrt[6]{2}\sigma,$$

*gsmith2@cluster2.mse.utah.edu

 ©2009 The American Physical Society

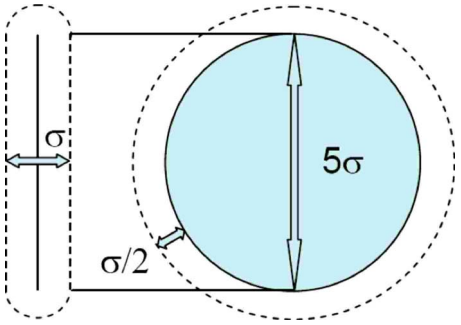

FIG. 1. (Color online) Schematic representation of the soft spherocylinder (SSC) nematogen and spherical nanoparticle (NP) utilized in our simulations. The shaded region represents the hard-core diameter, while the dashed boundaries indicate the onset of repulsive interactions.

$$U = 0 \quad \text{otherwise}. \tag{1}$$

with ε and σ being the energy and length scales, respectively. For interaction between two SSCs, r is the minimum distance between the two line segments describing the SSCs and $R_h=0$; for interaction between a SSC and a NP, r is the minimum distance between the SSC line segment and the center of mass of the NP and $R_h=D_{\mathrm{NP}}/2$; finally, for NP-NP interactions, r is the center-of-mass separation of two NPs while $R_h=D_{\mathrm{NP}}$. All simulation results are presented in reduced units based on the energy scale ε and the length scale σ [13]. Since the potential given by Eq. (1) is purely repulsive, interactions in our system are primarily entropic in origin. A time reversible, quarternion based algorithm for rigid-body MD simulations proposed by Matubayasi and Nakahar [14] was implemented in this work. The Nose-Hoover [15,16] thermostat and Berendsen [17] barostat were utilized to carry out constant volume and temperature (*NVT*) and constant pressure and temperature (*NPT*) ensemble simulations. Simulations were performed at $T=2$ for systems of 10 000 SSCs using periodic boundary conditions, with an integration time step $\Delta t=0.001$. The number of NPs varied from 0 to 500, corresponding to the NP concentrations f_{NP} and volume fractions ϕ_{NP} given in Table I. Initial configurations were generated by random placement of the SSCs and NPs in a low-density simulation cell with subsequent increase in density (decrease in cell dimension) to liquidlike densities over several million time steps. Each system was then equilibrated for several million time steps (up to 30 million), allowing for complete orientational decorrelation of the SSCs and diffusion of the NPs over distances several times their diameter. Sampling runs consisted of 40 million time steps to 150 million time steps depending upon the system.

The orientational ordering of nematogens is described by the ordering tensor [18]

$$\langle Q_{\alpha\beta}\rangle = \left\langle \frac{1}{N}\sum_{i=1}^{N}\frac{3}{2}\left(u_\alpha^i u_\beta^i - \frac{1}{2}\delta_{\alpha\beta}\right)\right\rangle, \tag{2}$$

where $u_\alpha^i(\alpha=x,y,z)$ is the αth Cartesian component of a unit vector along the long axis of the ith LC molecule, $\delta_{\alpha\beta}$ is the Kronecker δ function and the sum is over all SSCs in the simulation cell. The average (over all trajectory points) of the largest eigenvalue S of the ordering tensor, $\langle S\rangle$, is the uniaxial order parameter of the ensemble, referred to throughout this paper simply as the system orientational order parameter.

III. RESULTS AND DISCUSSION

A. Single- and two-particle behavior

In order to quantify the influence of a single NP on the LC matrix, we determined the orientational order parameter within spherical shells around the NP. In this analysis the local order parameter is determined for all SSCs whose center-of-mass separation from the center of mass of the NP, r, is within a shell described by $r_s-\Delta r_s \leqslant r \leqslant r_s$, where r_s is the radius of the shell centered on the NP center of mass. The

TABLE I. Isotropic-nematic transition pressure.

Number of NP	ϕ_{NP} ($P=2.4$)[a]	f_{NP}[b]	P_{IN} from $\langle S\rangle$ vs P	P_{IN} from density fluctuations
0	0	0	2.49	N/A
10	0.0128	0.000999	2.50	2.50
20	0.0253	0.00200	2.52	2.48
30	0.0375	0.00299	2.50	2.50
40	0.0494	0.00398	2.52	2.52
60	0.0723	0.00596	2.54	2.53
100	0.115	0.0990	2.58	2.58
150	0.163	0.0148	2.67	2.67
300	0.280	0.0291	2.89	2.88
500	0.394	0.0476	No nematic phase observed	

[a]Nanoparticle volume fraction. The nanoparticle volume is estimated as the difference in volume between the mixture for each number of nanoparticles and the pure SSC at $P=2.4$.
[b]Number fraction of nanoparticles.

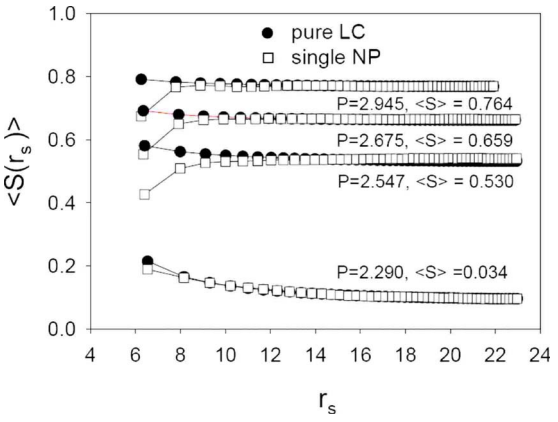

FIG. 2. (Color online) The local orientational order parameter in shells (see text for definition) surrounding a single nanoparticle or equivalent shells in a system without nanoparticles as a function of the shell radius for various pressures. Also given is the system orientational order parameter for each pressure.

shell thickness Δr_s varies with r_s in order to maintain a constant average number of NPs (100) within each shell. The same analysis was also performed for the pure LC system. We note that this analysis consists of determining the order parameter for the SSCs within each shell by applying Eq. (2) and does not consider (directly) the orientation of the SSCs with respect to the NP surface. The weak dependence of the local order parameter on shell radius for small r_s in the pure nematic reflects the increasing thickness of the shell required to maintain a constant average number of NPs within the shell with decreasing radius. In the limit of small radius, the local order parameter will converge to that for a sphere containing 100 NPs.

The order parameter within each shell is shown in Fig. 2 as a function of shell radius for several pressures for both the single NP and pure LC systems. Also given in Fig. 2 is the system orientational order parameter $\langle S \rangle$ obtained by applying Eq. (2) applied to all SSCs in the system as a function of pressure. Within computational uncertainty, the presence of a single NP had no influence on the system order parameter. At low pressure ($P=2.290$ in Fig. 2) where the LC matrix is isotropic ($\langle S \rangle = 0.034$), it can be seen that the NP has almost no influence on the local order parameter of the matrix compared to the pure LC system. A very slight decrease in orientational order can be seen for the shell in contact with the NP surface. At higher pressures, the matrix undergoes an isotropic-to-nematic transition as revealed by the system order parameter and discussed in detail below. A reduction in the local order parameter for nematogens near the NP surface can be seen in the nematic matrix. Again, the influence of the NP on orientational order in the LC matrix is short ranged.

We believe that the short-range disruptive influence of the NP on local orientational order in the LC matrix is due to frustrated planar anchoring of the SSCs near the NP, as discussed in our previous work [10,11]. Due to entropic effects, our SSC nematogens prefer planar anchoring at a repulsive solid interface. However, because the NP size ($D_{NP}=5\sigma$) is comparable to the length of the SSCs ($L_{SSC}=5\sigma$), the NP is large enough to influence the local structure of the LCs but is too small to allow formation of well-defined planar wetting layers. Figure 3(a) shows the radial distribution function (RDF) $g_{NP\text{-}SSC}(r)$ for the nematogens around the single NP as a function of the separation between the center of mass of the NP and the center of mass of the SSC. Figure 3(b) shows a polar measure of the average orientation of the SSCs relative to the vector between their center of mass and that of the NP as a function NP-SSC separation, namely

$$P_2(r) = \frac{1}{2}\langle 3\cos^2\theta - 1\rangle. \tag{3}$$

Here θ is the angle formed between the vector connecting the centers of mass of the NP and SSC and the molecular vector of the LC molecule as shown in Fig. 3(c). Perfect planar anchoring yields $\langle P_2 \rangle = -0.5$, perfect homeotropic anchoring $\langle P_2 \rangle = 1.0$, and random orientation yields $\langle P_2 \rangle = 0$.

The NP-SSC RDF [Fig. 3(a)] shows a strong preference for NP-SSC separations of about 3.5σ. Fig. 3(b) reveals that these SSCs are perpendicular to the NP-SSC vector, as illustrated in Fig. 3(c), and hence exhibit planar anchoring. However, the tendency for planar orientation of the SSCs propagates only a short distance from the surface. At low pressure (isotropic matrix), there is some tendency for planar orientation out to around 10σ. Above P_{IN}, i.e., in the nematic matrix, the preference for NP-SSC separations around 3.5σ decreases, the range of net planar alignment decreases, and the preference for separations of about 6σ increases. As revealed in Fig. 3(b), the latter can be associated with a tendency for alignment of the SSCs parallel to the NP-SSC vector, or homeotropic alignment, as illustrated in Fig. 3(c). While SSCs near the equator of the NP can align with the LC director and maintain planar alignment with respect to the NP surface, those near the poles (considering the system LC nematic director to define north-south) must assume homeotropic orientation in order to align with the LC nematic director that emerges at higher pressure (density).

Finally, an umbrella sampling method using a harmonic spring to sample overlapping windows (based upon NP-NP separation) combined with a self-consistent histogram analysis procedure [19] was employed in order to determine the potential of mean force (POMF) between two NPs in the isotropic phase of the SSC matrix as shown in Fig. 4(a). The POMF shown here is the free energy of the LC+2 NP system as a function of center-to-center separation of the NPs. Figure 4(a) indicates that matrix-induced interactions between the NPs are limited to separations of less than about $8-9\sigma$. This separation corresponds to configuration *A* in Fig. 4(b), where SSCs planar aligned with the two NPs can interact favorably. As the separation between NPs decreases, two layers of SSCs can no longer be accommodated between the NPs. In configuration *B*, a single layer of SSCs can exhibit planar alignment with both NPs simultaneously. A further decrease in separation forces out the SSC layer between the NPs until configuration *C* is reached. We believe the evacuated space between the NPs is entropically unfavorable and depletion interactions result in short-range attraction between the NPs until close contact is achieved (configuration *D*).

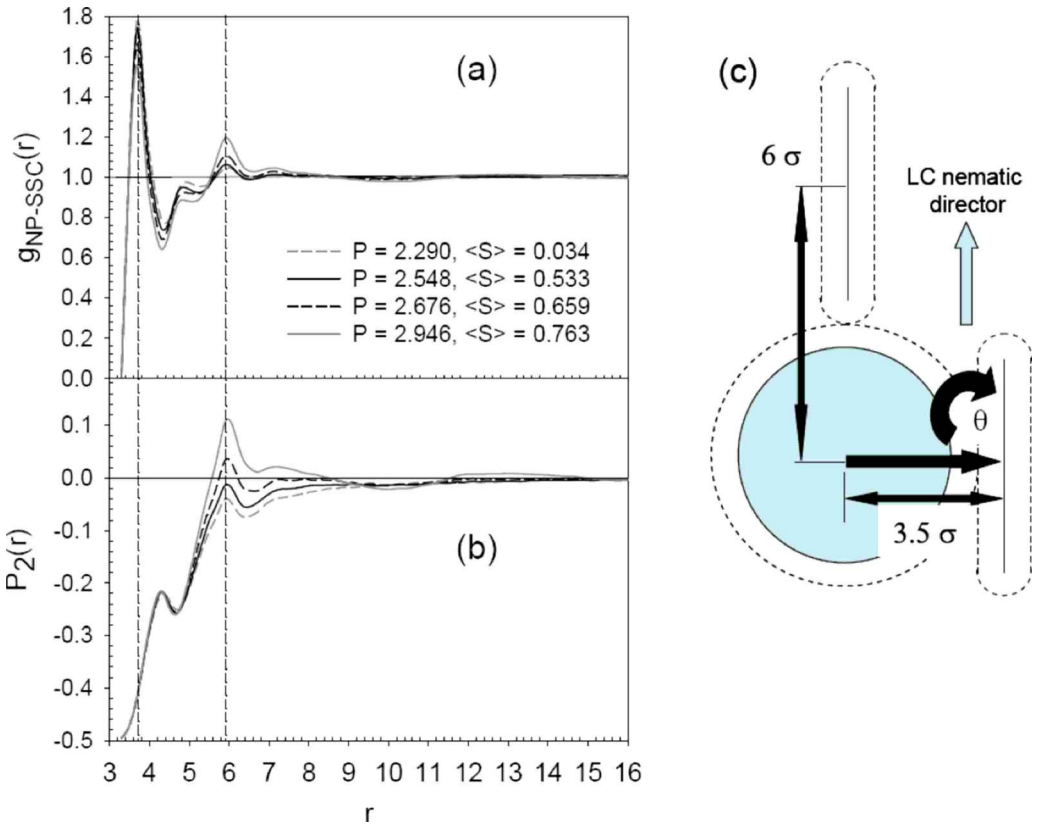

FIG. 3. (Color online) The nanoparticle-spherocylinder radial distribution function (a) and P_2 correlation function (b) as a function of the separation between the centers of mass of the nanoparticle and spherocylinder for various pressures. Also given is the system orientational order parameter for each pressure. The vertical lines indicate important separations corresponding to the nanoparticle-spherocylinder configurations shown in (c).

B. Stucture in the multiple nanoparticle suspensions

Experimentally, it has been observed that the presence of NPs comparable in size to nematogenic molecules suppresses the isotropic-nematic transition in LC matrices [2–4]. The same effect has been predicted in theoretical treatment of rod-sphere mixtures [7]. We observe similar effects in our model NP-LC system. Figure 5 shows the system order parameter $\langle S \rangle$ as a function of pressure for a wide range of nanoparticle concentrations. The *I-N* transition moves to higher pressure with increasing NP concentration and becomes less sharp. We have estimated P_{IN} as a function of NP concentration by associating the transition with the pressure at which the slope of $\langle S \rangle$ vs P increases sharply, as shown in Fig. 5. The resulting transition pressures are shown in Table I. P_{IN} for our pure SSC matrix is in good agreement with that obtained from Parson-Lee theory for soft repulsive nematogens with the same aspect ratio as our SSCs at $T^*=2$ [20]. Note that in our study the reduced pressure is defined as $P^*=P\sigma^3/\varepsilon$, while in Ref. [20] it is defined as $P^*=P\sigma^3/T^*\varepsilon$.

The NP-NP radial distribution function $g_{\text{NP-NP}}(r)$ is shown in Fig. 6(a) at $P=2.4$ for all NP concentrations investigated. This pressure lies below P_{IN} for all compositions (Fig. 5). There is no indication of long-range structure in the NP-NP RDF for pressures below P_{IN}, and the NPs are dispersed over the entire composition range. Figure 6(b) shows

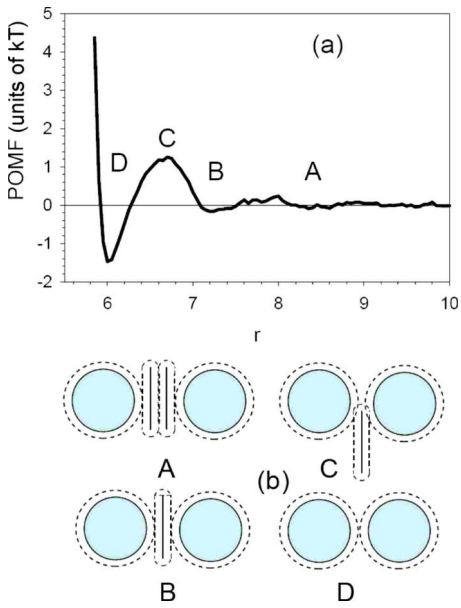

FIG. 4. (Color online) The potential of mean force (POMF) between two nanoparticles in the isotropic phase ($P=2.4$) of the spherocylinder matrix. Panel (b) emphasizes short-range interactions with labels corresponding to nanoparticle-spherocylinder configurations corresponding to those shown in (a).

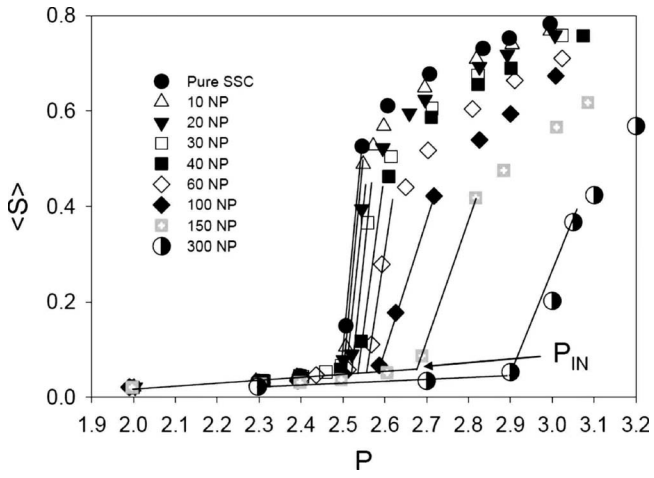

FIG. 5. The system orientational order parameter as a function of separation for various nanoparticle concentrations. The solid lines approximate the pressure dependence of the order parameter and allow for estimation of the isotropic-nematic transition pressure for each nanoparticle concentration as indicated in the figure.

$-\ln[g_{\text{NP-NP}}(r)]$, corresponding to the free energy as a function of separation between any two NPs (in units of kT) for each composition. Very close correspondence between $-\ln[g_{\text{NP-NP}}(r)]$ and the POMF for the two-NP system [Fig. 4(a)] can be seen. It is clear that the high probability for

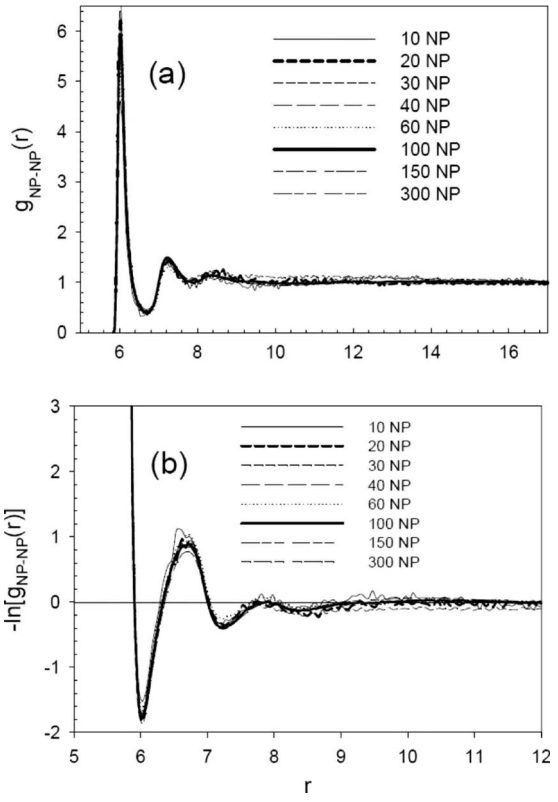

FIG. 6. The nanoparticle-nanoparticle radial distribution function (a) and the corresponding free energy [(b) in units of kT] in the isotropic phase of the spherocylinders matrix ($P=2.4$) for various nanoparticle concentrations. The radial distribution functions have been scaled by $1/(1-1/N)$, where N is the number of nanoparticles.

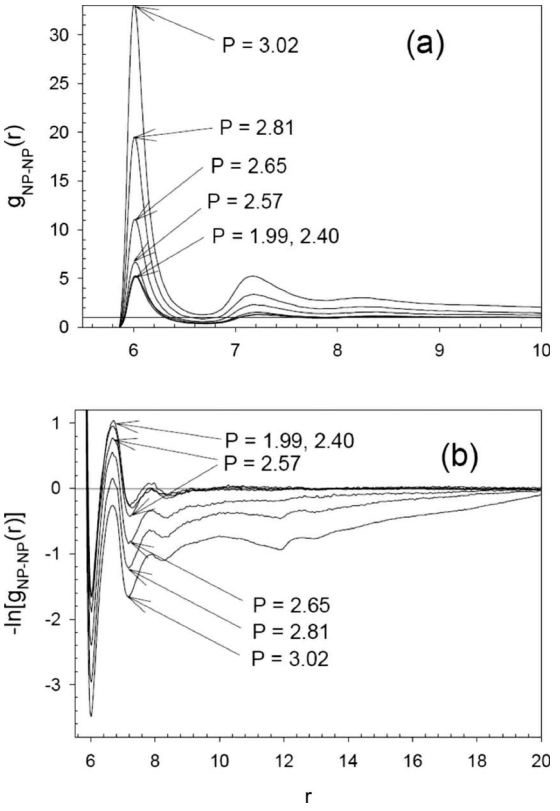

FIG. 7. The nanoparticle-nanoparticle radial distribution function (a) and the corresponding free energy [(b) in units of kT] for the system of 60 nanoparticles for various pressures. The radial distribution functions have been scaled by $1/(1-1/N)$, where N is the number of nanoparticles.

NP-NP separations around 6σ (close NP-NP contact) observed in $g_{\text{NP-NP}}(r)$ is driven by the short-range depletion interactions discussed above. Furthermore, the NP-NP RDF (and hence $-\ln[g_{\text{NP-NP}}(r)]$) shows little dependence on composition for the range of compositions investigated. It appears that NP-NP interactions in the isotropic phase of the LC matrix can be well described with an effective two-body interaction given by the POMF [Fig. 4(a)] up to quite high NP concentrations.

Finally, the NP-NP RDFs for 60 NPs in the 10 000 SSC matrix are shown in Fig. 7(a) for selected pressures. At low pressures corresponding to the isotropic phase of the matrix ($P \leqslant 2.54$, see Fig. 5 and Table I), the RDFs show very little pressure dependence and only short-range structure is seen in the RDFs. When the pressure increases above P_{IN}, the matrix becomes nematic (Fig. 5) and the NP-NP RDFs reveal increasing aggregation of the NPs, indicating that the NPs are likely excluded from the nematic matrix. The nematic matrix induces increasingly attractive interactions between NPs as shown in Fig. 7(b), where $-\ln[g_{\text{NP-NP}}(r)]$, or the free energy as a function of separation between any two NPs, is shown. The apparent phase separation that occurs for $P > P_{IN}$ can be observed in Fig. 8, where simulation snapshots illustrate the system with 60 NPs at four different pressures. At $P=2.30$, the SSCs are in the isotropic phase and the NPs are uniformly dispersed. At $P=2.59$, the matrix is beginning to exhibit significant orientational order ($\langle S \rangle = 0.28$), and some

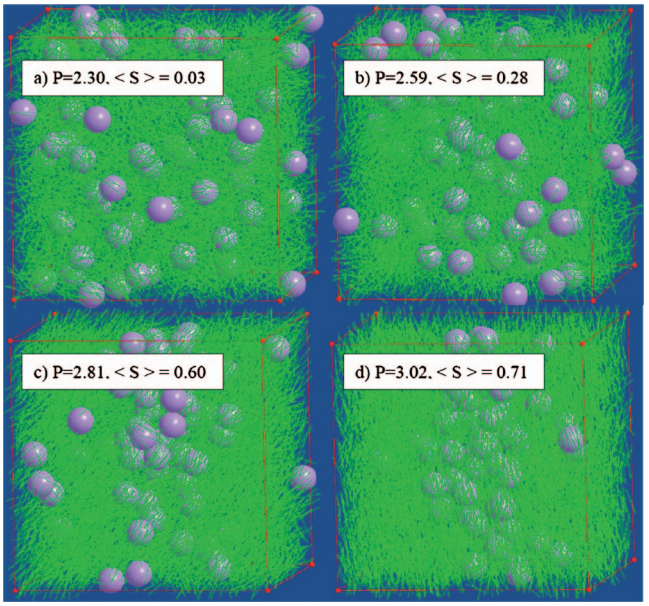

FIG. 8. (Color) Simulation snapshots for the system containing 60 nanoparticles at various pressures. The nanoparticles are represented as spheres with a diameter of 5σ and the spherocylinders as lines of length 5σ.

clustering of the NPs can be seen. Aggregation of the NPs is clearly apparent at the higher pressures. The NPs do not appear to form a crystalline phase but rather a NP-rich fluid phase that includes some LC molecules. This is also indicated by Fig. 7, where no strong preference for separations of 10σ and 12σ is observed. These separations correspond to next-nearest-neighbor distances in a close-packed cluster with nearest-neighbor separation of 6σ.

C. Phase behavior

Experimental studies of nanometer-scale inverse micelles dispersed in thermotropic LCs [2,3] reveal phase separation into a LC-rich nematic phase and NP-rich isotropic phase upon cooling below the *I-N* temperature. Increasing concentration of nanoscopic impurities delays the onset of the *I-N* transition, moving it to lower temperatures. Additionally, a homogeneous nematic phase has been observed at low NP concentration, in which the NPs are uniformly dispersed in the nematic LC matrix. The behavior observed in our model NP-LC system, specifically increasing aggregation of NPs for $P > P_{IN}$ and an apparent increase in P_{IN} with increasing NP concentration, are in qualitative agreement with experimentally observed behavior for nanodroplet suspensions in LC matrices. In order to better understand the phase behavior of our model as a function of composition and pressure, we have estimated both binodal and spinodal lines by analyzing density fluctuations in our systems. The significant difference in shape and volume between LC nematogens and NPs makes implementation of conventional extended ensemble simulation techniques for calculation of phase equilibrium (e.g., Gibbs ensemble simulations) quite challenging. Therefore, we based our estimation of phase equilibrium boundaries using phenomenological (albeit less rigorous) analysis. In this approach, we relied on the following assumptions and/or observations.

(1) The *I-N* transition can be quite accurately determined by monitoring the matrix nematic order parameter as a function of thermodynamic conditions (e.g., pressure along an isotherm). Unlike the vapor-liquid transition, where density and enthalpy differences between two coexisting phases are large and therefore large hysteresis can be observed in determining the exact location of the phase transition along the thermodynamic path, the *I-N* transition is usually accompanied by a very modest density change (a few percent) and therefore very narrow hysteresis is observed in this case. We have demonstrated this for related systems in our previous work [21].

(2) We believe that analysis similar in spirit to the one proposed by Rovere *et al.* [22] that examines density distributions of nematogens and nanoparticles in subcells can provide important insight into phase equilibrium. First, following ideas proposed by Martynov [23] that instability of a given phase should become apparent inside the two phase region even if the second phase is not present (metastable conditions), we monitored the width of density fluctuations along a thermodynamic path (isotherm) for each composition. Second, for thermodynamic conditions inside the spinodal locus, we expect the system to undergo spinodal decomposition. However, due to the limited length of the simulation trajectories, the finite size of the system, and relatively low mobility of constituents in our systems (and hence slow structural relaxations), we do not expect our systems to form two phases that correspond to bimodal conditions. Therefore, we believe that the two "phases" observed in subcells during spinodal decomposition can be considered characteristic of spinodal conditions.

D. Density fluctuations

Fluctuations in number density were determined for both SSCs and NPs by analyzing subcells of the simulation cell. A subcell is a cubic cell of size L_{cell}. A large number of subcells is randomly placed within the simulation cell for each trajectory point and the number of SSCs and NPs whose center of mass is within the subcell, N_{SSC} and N_{NP}, is determined. The distribution of the number of SSCs and NPs in subcells of size 8σ and 23σ, respectively, were determined. It was found empirically that these sizes for the subcells provided the optimal number distributions for estimating the spinodal compositions. When the system is a single homogeneous phase, the density distributions of SSCs and NPs within the subcells are expected to be Gaussian. When the system lies within the spinodal envelope, the density distributions will reflect density distributions for SSC-rich and NP-rich phases (spinodals). In principle, the distributions can be decomposed (e.g., into the sum of two Gaussian functions) to determine the spinodal points for the given thermodynamic conditions (T,P). In practice, we found that the SSC distribution, even when the system is a single phase, was not well described by a Gaussian but is in fact skewed toward the low-density side of the distribution, as illustrated in Fig. 9(a). This asymmetry in the SSC density distribution may be due to the very dif-

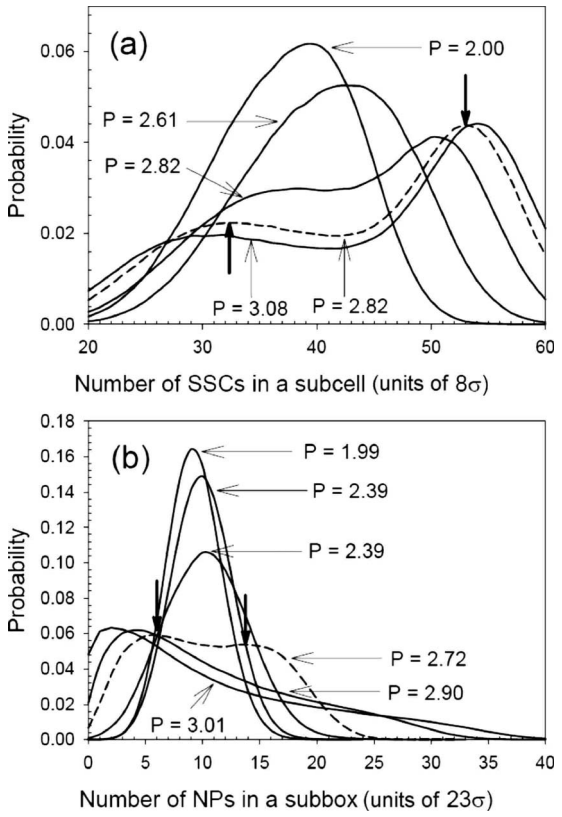

FIG. 9. The distribution of the number of (a) spherocylinders in subcells of size 8σ for the 150 NP system and (b) distribution of the number of nanoparticles in subcells of size 23σ for the system of 100 NP at various pressures. The bold arrows indicate the estimated number of SSCs or NPs corresponding to the spinodals for the pressure whose distributions are given by the dashed lines.

ferent shapes and packing characteristics of the SSCs and NPs. Nevertheless, it is possible to estimate the spinodal compositions at higher pressures where two peaks emerge in the density distributions, as illustrated in Figs. 9(a) and 9(b). The estimated spinodal points are shown in Fig. 10.

In order to estimate the bimodal (coexistence) points, we carried out simulations over a wide range of pressures for each composition. The standard deviation (SD) in the density distributions for SSCs in 8σ subcells [e.g., Fig. 9(a)] was determined and is shown in Fig. 11 as a function of pressure for each composition. We identified the transition pressure P_{IN} with the pressure at which the pressure dependence of SD increased dramatically, as shown in Fig. 11. The resulting transition pressures are compared with those obtained from the pressure dependence of $\langle S \rangle$ (Fig. 5) in Table I. Good agreement can be seen for all compositions.

E. Phase diagram

Figure 10 is the phase diagram for our NP-LC system showing estimated spinodal points, the *I-N* coexistence curve (binodal) and the phase state of each pressure and composition simulated. We note that for the system with 500 NP (ϕ_{NP}=0.394), we did not observe a nematic phase but rather the system underwent a transition from isotropic to smectic

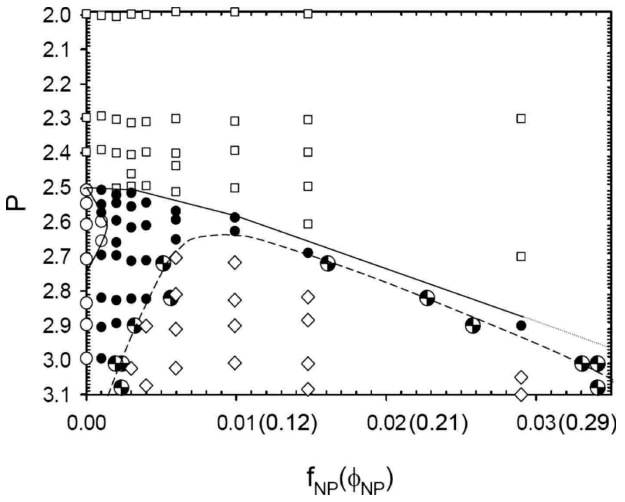

FIG. 10. Phase diagram for the nanoparticle-spherocylinder system. The abscissa shows the number fraction of nanoparticles with the volume fraction (see Table I) given in parentheses. The solid lines correspond to estimated phase boundaries (binodal lines). The dashed line delineates the estimated spinodal envelope while the dotted line is a possible extension of the phase boundary to higher nanoparticle concentration. Open squares are single phase systems with an isotropic LC matrix, open circles are single phase systems with a nematic LC matrix, filled circles are two-phase systems outside of the spinodal envelope and open diamonds are two-phase systems within the spinodal envelope. The half-filled circles are spinodal points estimated from the density distribution of nanoparticles and spherocylinders for systems lying inside the spinodal envelope (see text).

for pressures $P > 3.1$. Systems were determined to be single-phase isotropic if their pressure was less than P_{IN} (for a given composition) determined from width of the density distribution for SSCs in 8σ subcells as discussed above. For the pure LC system P_{IN} was determined from the pressure dependence of the orientational order parameter (Fig. 5). Systems

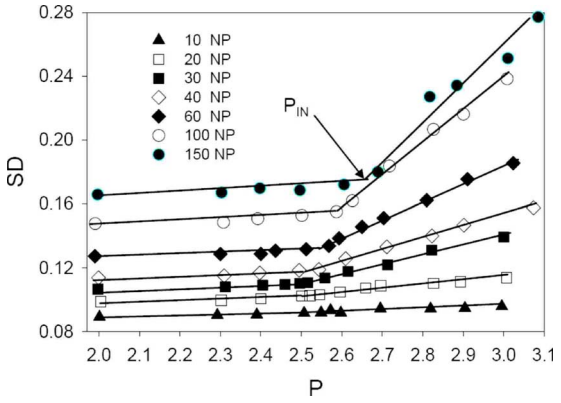

FIG. 11. (Color online) The standard deviation in the number of spherocylinders in a subcell of size 8σ normalized by the mean number of spherocylinders as a function of pressure for various nanoparticle concentrations. The solid lines are estimates of the pressure dependence of the density fluctuations that allow for estimation of the isotropic-nematic transition pressure P_{NI} as indicated in the figure.

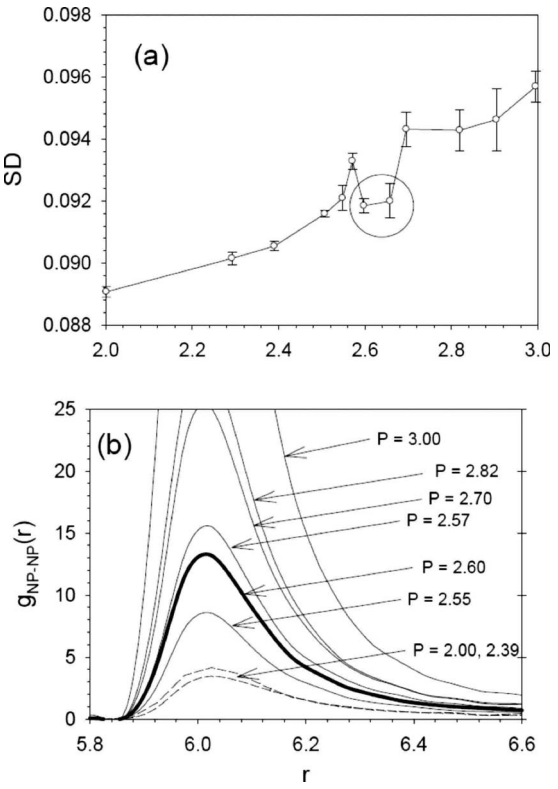

FIG. 12. Panel (a) shows the standard deviation in the number of spherocylinders in a subcell of size 8σ normalized by the mean number of spherocylinders as a function of pressure for the 10 NP system. Also shown are 95% confidence intervals based upon 4×10^7 or 8×10^7 integration steps, depending upon pressure. Panel (b) shows the nanoparticle-nanoparticle radial distribution function for the same system at various pressures.

were determined to be nematic (pure LC system) or two phase (NP-LC systems) when $P>P_{IN}$. Finally, systems were determined to lie within the spinodal curves when the emergence of a two peak distribution in the density of SSCs in the 8σ subcells could be observed based upon the existence of multiple inflection points on the low-density flank of the distributions.

The behavior observed for our lyotropic system with increasing pressure and NP concentration is quite similar to that seen for nanodroplets in liquid crystal matrices with decreasing temperature [2–4]. This may even include a nematic phase window with finite NP concentration as observed experimentally. We have tentatively identified the system with 10 NPs ($f_{NP}=0.001$, $\phi_{NP}=0.0128$) at $P=2.60$ and 2.65 as a single phase nematic, as shown in Fig. 10, in which the NPs are incorporated homogenously within the nematic LC matrix. This assignment is based upon detailed analysis of the standard deviation in the density distribution for SSCs in the 8σ subcells for this system, as shown in Fig. 12(a). We have assigned the pressures $P=2.51$, 2.55, and 2.57 to the two-phase region as shown in Fig. 10 due to the increased dependence of the width of the density distribution on pressure for $P>2.5$. However, we see a sharp decrease in the width for $P=2.60$. This effect seems to be greater than the uncertainty in the width of the distribution based upon analysis of the trajectory of 80×10^6 integration steps. At higher pressure, the width increases again, indicative of two-phase behavior. Such behavior is not observed for any of the higher NP concentrations.

We note that evidence of a single nematic phase is also seen in the NP-NP RDF for the 10 NP system shown in Fig. 12(b). The increasing magnitude of the first peak in the RDF for $P>2.50$ is indicative of increasing particle aggregation consistent with two-phase behavior. However, the first peak for $P=2.60$, which we believe corresponds to a single nematic phase, is smaller in magnitude than that for $P=2.57$. For pressures greater than 2.65 the first peak increases rapidly with increasing pressure, indicative of increasing NP aggregation.

F. Anchoring effects

As discussed above, our purely repulsive SSC model favors planar anchoring at the NP surface. In order to investigate the role of anchoring conditions on the phase behavior of the NP-SSC system, we have modified the NP-SSC interaction to induce homeotropic anchoring. An interaction between the center of mass of the SSC and the center of mass of a NP of the form

$$U=4\varepsilon\left[\left(\frac{\sigma}{t-d}\right)^{12}-\left(\frac{\sigma}{t-d}\right)^{6}+\frac{1}{4}\right] \quad \text{for } (t-d)<\sqrt[6]{2}\sigma,$$

$$U=0 \quad \text{otherwise} \tag{4}$$

was added to the interaction potential given by Eq. (1). Here, t is the distance between the centers of mass of the SSC and the NP and $d=D_{NP}/2+a$, where D_{NP} is the hard-core diameter of the NP, and a is a parameter which determines how closely the center of mass of the SSC can approach the NP. This potential results in a large excluded volume penalty for the center of mass to approach within $d+\sigma$ of the center of mass of the NP. The tendency for homeotropic anchoring increases with a for $0\leqslant a\leqslant 2.5\sigma$, with a value of $a=2.5\sigma$ allowing NP-SSC contact only when the SSCs are aligned parallel to the vector connecting the centers of mass of the SSC and NP. For values of $a<2.5\sigma$, close contact can be achieved for SSCs that are increasingly planar in their alignment. We used a value of $a=0.5\sigma$ which constrains the NP-SSC center-of-mass distance to be greater than 4σ, as shown in Fig. 13(a), the NP-SSC RDF for a single NP in the isotropic phase of the LC matrix. The geometry of the "closest contact" configuration of the SSC is shown in Fig. 13(b). In contrast to the frustrated planar anchoring configuration discussed above (see Fig. 3), the SSC in the closest contact configuration is no longer aligned perpendicular to the NP-SSC vector. Consequently, the $P_2(r)$ function at the close contact distance (4σ) reflects a much weaker tendency for planar alignment than observed for the original potential. Furthermore, the range of net planar alignment is significantly reduced ($<5.2\sigma$) by the additional potential function, and the tendency for NP-SSC center-of-mass separations and the net tendency for homotropic alignment at this separation is significantly increased by the additional potential. We will

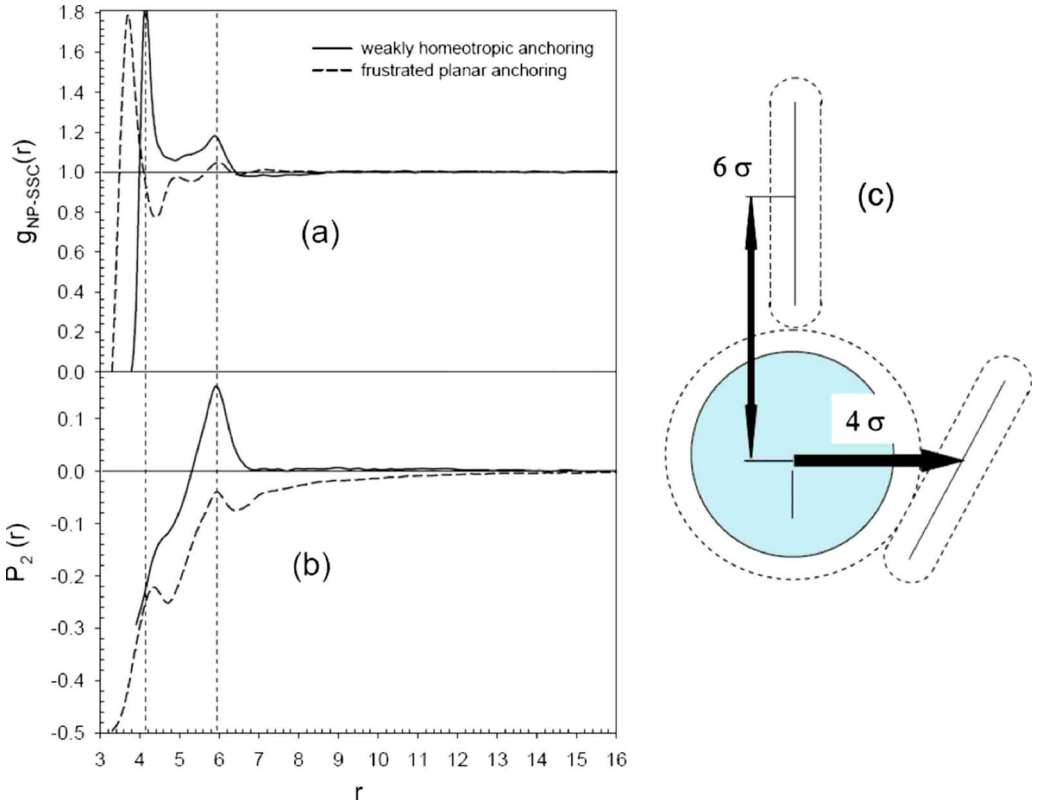

FIG. 13. (Color online) The nanoparticle-spherocylinder radial distribution function (a) and P_2 correlation function (b) as a function of the separation between the centers of mass of the nanoparticle and spherocylinders at $P=2.3$ for frustrated planar and weak homeotropic anchoring. The vertical lines indicate important separations corresponding to the nanoparticle-spherocylinder configurations shown in (c).

refer to this anchoring condition as weak homoetropic anchoring.

The potential of mean force for two NPs with weak homeotropic anchoring in the isotropic phase of the SSC matrix ($P=2.4$) is compared with that for frustrated planar anchoring in Fig. 14(a). The contact minimum (at 6σ) is slightly deeper for the weak homeotropic anchoring. However, there is significant intermediate range matrix-induced repulsion between the two NPs for $7\sigma<r<15\sigma$. In this range of separation, there is increasing overlap (with decreasing separation) of the homeotropically anchored solvation shell of the NPs. It becomes increasingly difficult for SSCs lying between the NPs to satisfy homeotropic anchoring conditions with decreasing separation, particularly for separations less than about 10σ where SSCs must interact with both particles simultaneously.

As discussed above, the interaction between NPs in the isotropic phase of the SSC matrix can be well described by the two-particle POMF over a wide range of NP concentration for the case of frustrated planar anchoring, and no tendency for NP aggregation and/or phase separation is observed. Based upon the two-particle POMF for weak homeotropic anchoring, we anticipated similar behavior in the isotropic SSC matrix. In fact, simulations of a system comprised of NPs without SSCs (implicit matrix), utilizing the POMF shown in Fig. 14(a) (weak homeotropic) as an effective NP-NP interaction, do in fact yield distributed NPs, as shown in Fig. 14(c). However, simulations at $P=2.3$ (isotropic matrix) with both 10 and 100 NPs with weak homeotropic anchoring show significant aggregation as illustrated in the representative system configurations shown in Fig. 15 for 100 NPs. In contrast to what was found for frustrated planar anchoring [compare Fig. 15(a) and Fig. 15(b)], the NPs with weak homeotropic anchoring exhibit significant aggregation in the isotropic matrix. Furthermore, the NP-NP RDF for weak homeotropic anchoring is strongly dependent upon the concentration of NPs, in stark contrast to the behavior observed for frustrated planar anchoring (e.g., Fig. 6). Comparing the free energy as a function of NP separation $[-\ln(g_{NP\text{-}NP})]$ for finite NP concentrations with the two-particle POMF, as shown in Fig. 14(b), reveals that the intermediate range repulsion between NPs is strongly suppressed at finite concentrations. The free energy obtained from the implicit solvent simulations reveals that this suppression is not primarily a packing effect due to finite NP concentration but in fact reflects perturbation of the matrix-induced NP-NP interactions. We believe this is due to overlap of SSC solvation shells at finite NP concentrations. Each NP is effectively $15-18\sigma$ (NP+homeotropic solvation shell) in diameter, and even 10 NPs in our system of 10 000 SSCs (box size around 48σ) display significant many-body interactions that strongly influence the solvation of the NPs and their matrix-induced interactions. The emergence of high probabilities of NP-NP separations corresponding to 10σ and 12σ in Fig. 14(b) for weak homeotropic anchoring indicates that close-packed, crystallinelike order may emerge in the NP-rich phase that coexists with the SSC-rich isotropic phase.

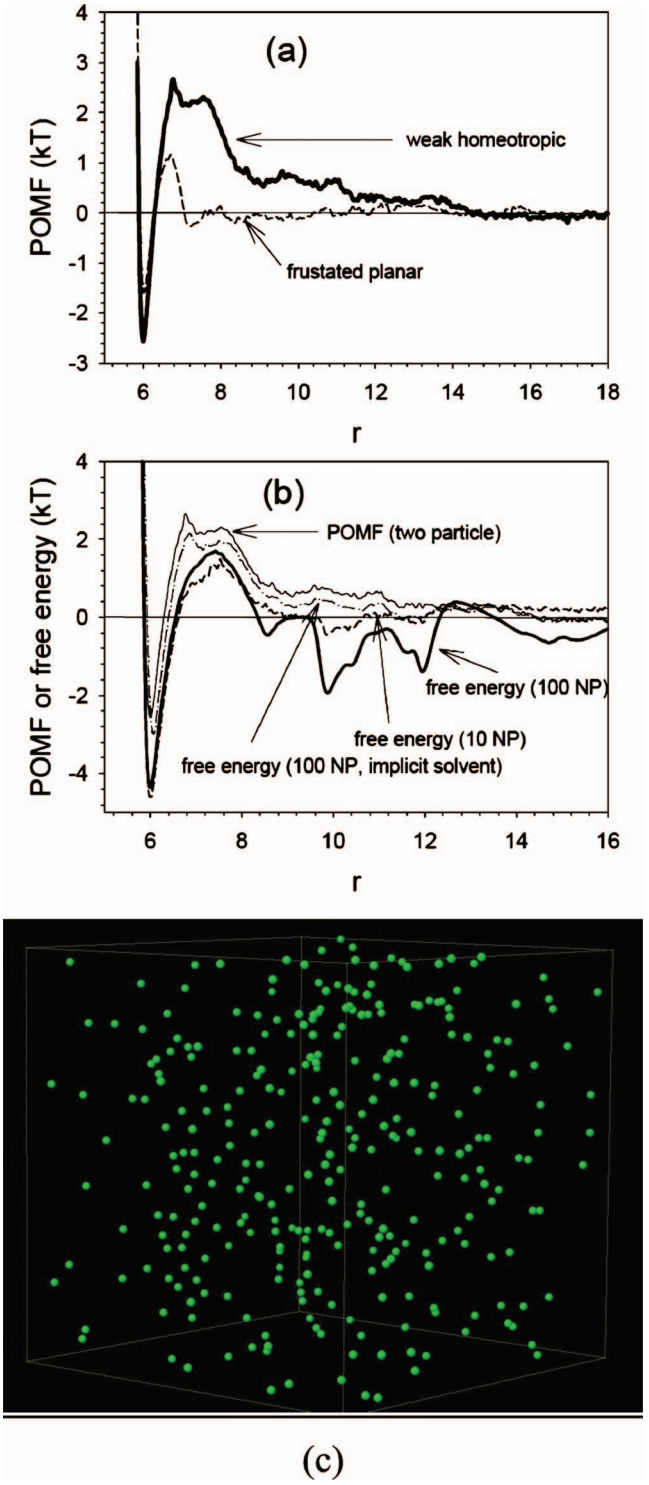

FIG. 14. (Color) (a) Potential of mean force determined at $P=2.4$ (isotropic matrix) for two NPs with frustrated planar anchoring and weak homeotropic anchoring. (b) The free energy as a function of NP separation for weak homeotropic anchoring for systems with 10 and 100 NPs. Also shown is the two-particle POMF and the free energy obtained for implicit matrix simulations with 100 NPs utilizing the two-particle POMF as the NP-NP interaction potential. (c) Representative snapshot from an implicit matrix simulation of NPs utilizing the two-body potential of mean force [weakly homeotropic anchoring, panel (a)] as the effective NP-NP interaction potential.

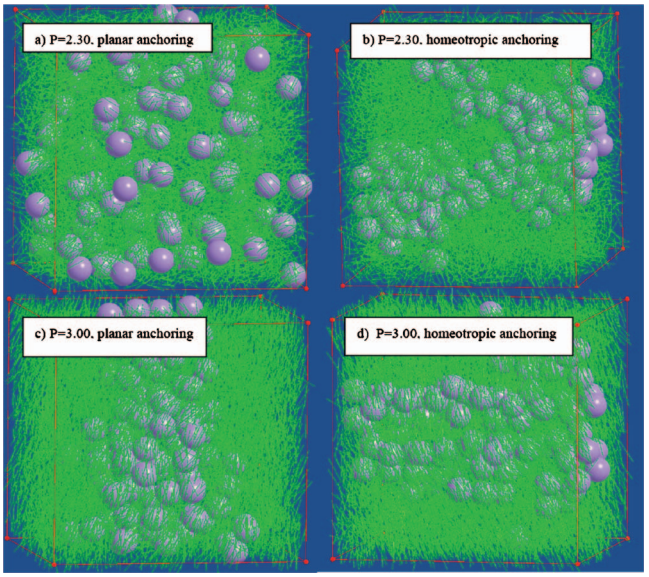

FIG. 15. (Color) Simulation snapshots for the system containing 100 nanoparticles at simulation pressures corresponding to the isotropic ($P=2.30$) and nematic ($P=3.0$) phases of the LC matrix for frustrated planar and weak homeotropic anchoring. The nanoparticles are represented as spheres with a diameter of 5σ and the spherocylinders as lines of length 5σ.

In the nematic phase of the LC matrix, we find strong aggregation of the NPs with homeotropic anchoring conditions as was seen for planar anchoring conditions, as can be seen by comparing Figs. 15(c) and 15(d). However, it appears that the interface between the NP-rich phase and the NP-poor (nematic) phase has a different orientation with respect to the nematic director. Based upon theoretical treatments [5,6], we anticipate that the attractive potential between NPs in the nematic phase of the LC could be anisotropic due to anisotropy in the nematic itself, resulting in anisotropic orientation of the NP clusters after phase separation. In order to accommodate planar anchoring, it appears that the exposed (to the nematic phase) surface, or interface, of the NP cluster in Fig. 15(c) prefers to be along the nematic director, while with homeotropic anchoring it is favorable to have the cluster interface perpendicular to the nematic director as illustrated in Fig. 15(d).

IV. CONCLUSIONS

The phase diagram of NP-SSC mixtures shown in Fig. 10 exhibits several striking features. Of central importance is the observation that nematic ordering is inextricably linked to demixing in the NP-SSC mixtures, with phase separation into NP-rich and NP-poor phases occurring simultaneously with nematic ordering in the NP-poor phase. We also observe a nematic "pocket" at low NP concentration, with a rather low maximum NP concentration ($\sim 2\%$ volume fraction of NPs). Finally, we observe that the *I-N* transition pressure increases with increasing NP concentration; in other words, the transition to nematic order is shifted to higher pressures in SSC systems containing NP "impurities." Quite similar

features have been observed in experimental studies of water-surfactant-LC mixtures [3,4]. Most of the key features of the NP-SSC phase diagram (Fig. 10) can be understood qualitatively as arising from the fundamental incompatibility of a high NP concentration with nematic ordering. The presence of a finite density of NPs in a mesogenic medium tends to suppress or, for high enough NP concentrations, as observed in our simulations for 500 NPs, completely prevent the transition to a nematic phase. As the system is cooled (or, in the present case, compressed) below the bulk *I-N* transition temperature (above the *I-N* transition pressure), the thermodynamic driving force for nematic ordering increases, to the point where it becomes favorable for the system to phase separate into NP-rich and NP-poor phases, with the NP-poor phase developing nematic order. In this scenario, the reduction in free energy achieved by developing nematic order in the NP-poor phase compensates for the "osmotic" work required to concentrate NPs in the NP-rich phase. This simple physical picture seems to qualitatively explain the essential features of the phase behavior of both NP-SSC mixtures and water-in-LC microemulsions.

We also find that the nature of the interaction between the NP and the SSC strongly influences effective NP-NP interactions and phase behavior of the NP-SSC mixtures. Our simulations show that NP with planar anchoring remain well dispersed in the isotropic phase (for pressures below P_{IN}, the *I-N* transition pressure), which implies that the short-range depletion-type effective attraction between NPs seen in the POMF [region *D* in Fig. 4(a)] is not sufficiently strong to drive NP aggregation. This can be explicitly verified by computing the reduced second virial coefficient

$$B_2^* = B_2 \Big/ \frac{2}{3}\pi\sigma_{\text{eff}}^3, \tag{5}$$

where

$$B_2 = 2\pi \int_0^\infty dr r^2 (1 - e^{-v(r)/k_B T}) \tag{6}$$

is the "bare" second virial coefficient, $v(r)$ is the POMF as a function of NP separation and σ_{eff} is the effective hard-core diameter given as

$$\sigma_{\text{eff}} = \int_0^\infty dr\{1 - \exp[-v_{\text{rep}}(r)/k_B T]\}, \tag{7}$$

where we have treated the repulsive part of the potential $v_{\text{rep}}(r)$ as zero for all separations greater than the minimum in the POMF (contact minimum) and equal to the POMF, shifted upward so as to be zero at the contact minimum, for all separations less than or equal to the contact minimum. For NPs with planar anchoring at $P=2.4$, we obtain $B_2^*=0.93$, which is significantly larger than the critical value, $B_2^* \cong -1.5$ [24], indicating that the NP dispersions are thermodynamically stable in the isotropic LC medium. Evidently, the large repulsive core diameter ($\sim 6\sigma$) and the repulsive barrier in the POMF [region *C* in Fig. 4(a)] more than compensate for the deep but narrow attractive well. While it is possible that many-body interactions could destabilize NP dispersions, the good agreement between the POMF and $-\ln[g(r)]$ [Figs. 4(a) and 6(b)] and the fact that $g(r)$ is nearly independent of NP concentration in the isotropic phase (Fig. 6) implies that many-body interactions among NPs are negligibly small, at least in the case of planar anchoring.

Similar to the planar anchoring case, the POMF for two NPs in the isotropic LC ($P=2.4$) with weak homeotropic anchoring yields a positive reduced second virial coefficient, $B_2^*=4.6$, indicating that dispersions of NPs with homeotropic anchoring should be even more stable than those with planar anchoring. This is not really surprising, given the pronounced medium-range repulsion evident in the POMF for NPs with homeotropic anchoring [Fig. 14(a)]. Hence, at sufficient dilution, we anticipate that NPs with weak homeotropic anchoring will remain dispersed in isotropic LC matrix. However, as evidence for significant many-body interactions exist at concentrations as low as 10 NPs/10 000 SSCs, as indicated by the aggregation observed at this concentration and the significant aggregation observed in the more concentrated 100 NP system. Even with 10 NPs, significant overlap of the SSC solvation shells seems to be indicated, resulting in disruption of the intermediate range repulsion and aggregation of the NPs.

ACKNOWLEDGMENTS

This work was supported by NSF MRSEC Grant No. DMR-1536145. We thank Noel Clark and Tommaso Bellini for helpful discussions.

[1] T. Hegman, H. Qi, and V. M. Marx, J. Inorg. Organomet. Polym. Mater. **17**, 483 (2007).
[2] J. Yamamoto and H. Tanaka, Nature (London) **409**, 321 (2001).
[3] T. Bellini, M. Caggioni, N. A. Clark, F. Mantegazza, A. Maritan, and A. Pelizzola, Phys. Rev. Lett. **91**, 085704 (2003).
[4] M. Caggioni, A. Giacometti, T. Bellini, N. A. Clark, F. Mantegazza, and A. Maritan, J. Chem. Phys. **122**, 214721 (2005).
[5] P. van der Schoot, J. Chem. Phys. **112**, 9132 (2000).
[6] P. van der Schoot, J. Chem. Phys. **117**, 3537 (2002).
[7] A. Cuetos, B. Martinez-Haya, S. Lago, and L. F. Rull, Phys. Rev. E **75**, 061701 (2007).
[8] P. Poulin, H. Stark, T. C. Lubensky, and D. A. Weitz, Science **275**, 1770 (1997).
[9] J. Loudet, P. Barols, and P. Poulin, Nature (London) **407**, 611 (2000).
[10] P. Tian, G. D. Smith, and M. A. Glaser, J. Chem. Phys. **124**, 161101 (2006).
[11] P. Tian and G. D. Smith, J. Chem. Phys. **124**, 184701 (2006).
[12] P. Tian, G. D. Smith, and M. Glaser, J. Chem. Phys. **128**

159901 (2008).
[13] M. P. Allen and D. J. Tildesley, *Computer Simulation of Liquids* (Clarendon, Oxford, 1989).
[14] N. Matubayasi and M. Nakahara, J. Chem. Phys. **110**, 3291 (1999).
[15] S. Nose, J. Chem. Phys. **81**, 511 (1984).
[16] W. G. Hoover, Phys. Rev. A **31**, 1695 (1985).
[17] H. J. C. Berendsen, J. P. M. Postma, W. F. van Gunsteren, A. DiNola, and J. R. Haak, J. Chem. Phys. **81**, 3684 (1984).
[18] P. G. de Gennes and J. Prost, *The Physics of Liquid Crystals*, 2nd ed. (Clarendon, Oxford, 1993).
[19] D. Smit and B. Frenkel, *Understandng Molecular Simulations*, 2nd ed. (Academic, New York, 2002).
[20] A. Cuetos, B. Martinez-Haya, S. Lago, and L. F. Rull, J. Phys. Chem. B **109**, 13720 (2005).
[21] P. Tian, D. Bedrov, G. D. Smith, and M. Glaser, J. Chem. Phys. **115**, 9055 (2001).
[22] M. Rovere, D. W. Heermann, and K. Binder, J. Phys.: Condens. Matter **2**, 7009 (1990).
[23] G. A. Martynov, Usp. Fiz. Nauk **169**, 595 (1999).
[24] M. G. Noro and D. Frenkel, J. Chem. Phys. **113**, 2941 (2000).